LETTER

Achieving Ultrahigh Piezoelectricity in Organic−Inorganic Vacancy-Ordered Halide Double Perovskites for Mechanical Energy Harvesting

Guangguang Huang, Asif Abdullah Khan, Md Masud Rana, Chao Xu, Shuhong Xu, Resul Saritas, Steven Zhang, Eihab Abdel-Rahmand, Pascal Turban, Soraya Ababou-Girard, Chunlei Wang,* and Dayan Ban*

Cite This: *ACS Energy Lett.* 2021, 6, 16−23

[Read Online]

ACCESS | Metrics & More | Article Recommendations | Supporting Information

ABSTRACT: Piezoelectric charge coefficient (d_{33}) and piezoelectric voltage coefficient (g_{33}) are the two most critical parameters that define output performance of piezoelectric nanogenerators (PNGs). Herein, we propose a vacancy-ordered double perovskite of $TMCM_2SnCl_6$ (where TMCM is trimethylchloromethylammonium) with a large d_{33} of 137 pC/N and g_{33} of 980×10^{-3} V·m/N. The piezoelectric coefficients are considered from the halogen-bonding-mediated synergistic movements of atomic displacement in inorganic $[SnCl_6]^{2-}$ octahedrons, as well as the molecular rotation of organic $TMCM^+$, which is revealed by a combined density functional theory (DFT) and experimental study. The $TMCM_2SnCl_6$ possesses a high saturated polarization (P_s) of 8.7 $\mu C/cm^2$, a high Curie temperature (T_c) of 365 K, and a low coercive field (E_c) of 0.6 kV/cm. The output voltage (V_{oc}) and current (I_{sc}) of the PNGs are 81 V and 2 μA at an applied mechanical excitation of (4.9 N, 40 Hz). We hope this work will provide guidance in energy harvesting by innovatively designing highly piezoelectric perovskites for the PNGs.
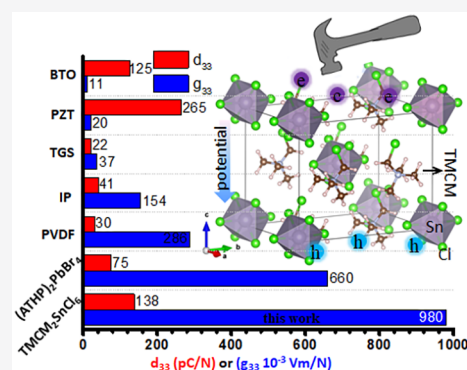
Piezoelectric nanogenerators (PNGs) have been emerging as a promising power source for self-powered electronics owing to their direct power conversion from mechanical to electrical energy.[1−5] To maximize the output power of PNGs, both the d_{33} and g_{33} of the piezoelectric host are important, which determines the output current ($I_{sc} = (d_{33} \times \Delta F)/\Delta t$, where ΔF is the applied force and Δt is the time) and voltage ($V_{oc} = g_{33} \times \Delta P \times L$, where ΔP is the applied pressure and L is the original film thickness), respectively.[6−9] In the past decade, a wide range of piezoelectric materials, targeting high g_{33} or d_{33}, have been synthesized for efficient PNGs. For example, the organic polyvinylidene fluoride (PVDF) possesses a high g_{33} ($\sim 286 \times 10^{-3}$ V·m/N), leading to a high output piezoelectric voltage. Unfortunately, the resultant current is limited because of its relatively low d_{33} (~ 30 pC/N).[10−13] Conversely, inorganic perovskite oxide ceramics, including $PbZr_xTi_{1-x}O_3$ (PZT) and $BaTiO_3$ (BTO), exhibit a high d_{33} (>100 pC/N) but their g_{33} is rather low ($\sim 20 \times 10^{-3}$ V·m/N).[14−18] Considering the relation between d_{33} and g_{33} ($g_{33} = d_{33}/(\varepsilon_0 \times \varepsilon_r)$), where ε_r is material relative

permittivity, it is challenging to improve d_{33} while maintaining a high g_{33} because the increase of d_{33} is usually associated with an even larger increase of ε_r.[19]

Organic−inorganic hybrid perovskites (OIHPs) combine the merits of both organic molecules and crystalline inorganic solids at a molecular level. The OIHPs were first introduced to solar cells (SCs) because of their excellent optical properties in 2009 and then adopted in piezoelectric reseach.[20−25] In 2015, the $MAPbI_3$ was first employed in PNGs, which yielded an output voltage and current density of 2.7 V and 140 nA/cm² at a pressure of 0.5 MPa.[26] Subsequently, a series of perovskites, including $MASnBr_3$, $FAPbBr_2I$, and Cl/Br-$MAPbI_3$, have been developed for efficient PNGs via the piezoelectric composite
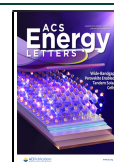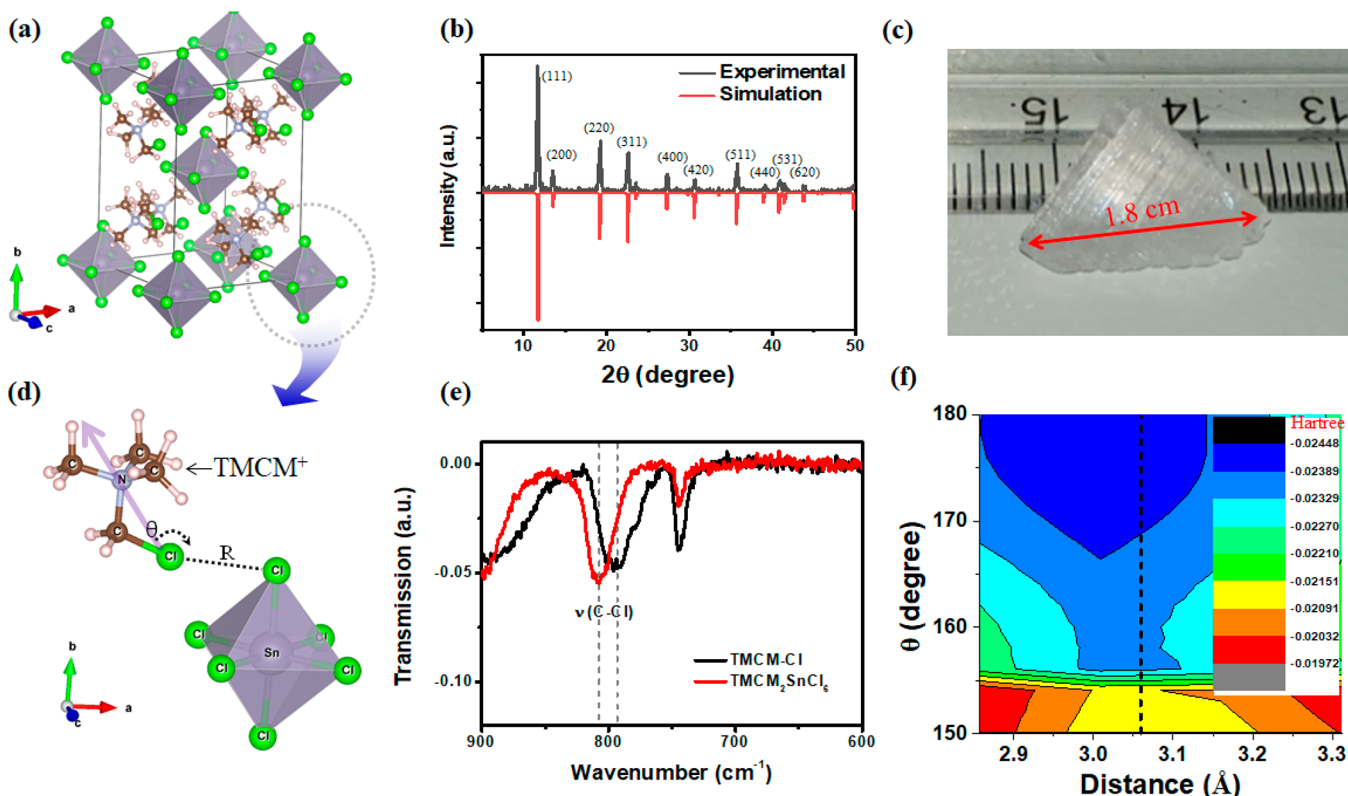
Figure 1. Crystal structure of $TMCM_2SnCl_6$ double perovskites: (a) structural model; (b) calculated and experimental XRD patterns; (c) digital photograph of single crystal; (d) halogen bonding interaction. The arrow from Cl to N indicates the dipole direction of $TMCM^+$. (e) FTIR spectra of pure TMCM-Cl molecules and $TMCM_2SnCl_6$; (f) calculated energy mapping of halogen bond for the simplified model in panel d.

films.[27−31] However, the aforementioned OIHPs evolved from the shadows of the SCs possess limited piezoelectric coefficients. Therefore, extensive efforts have been devoted to searching for highly piezoelectric OIHPs. Remarkably, one-dimensional ABX_3-type OIHPs with high d_{33}, including the TMCM-MnCl$_3$ and A-site mixed $(TMFM)_x(TMCM)_{1−x}CdCl_3$, were synthesized in 2017 and 2019, respectively.[32,33] Two-dimensional $(ATHP)_2PbBr_4$ OIHPs with large d_{33} of 75 pC/N and giant g_{33} of 660 × $10^{−3}$ V·m/N were reported in 2019.[34] In 2020, the OIHPs were further developed and successfully employed in energy-harvesting applications, including $(FMTMA)PbCl_2I$, HETMA-$CdCl_3$, $(TMFM)FeBr_4$, and $[Ph_3MeP]_4[Ni(NCS)_6]$.[35−38] Despite their large piezoelectric coefficients, the newly developed OIHPs may suffer substantial difficulties in mass production and implementation. For example, the TMCM-$MnCl_3$ has intrinsic chemical instability as the bivalent Mn is prone to be oxidized to tetravalent, while the Cd (or Pb) in $(TMFM)_x(TMCM)_{1−x}CdCl_3$ (or $(ATHP)_2PbBr_4$) is not environmental-friendly. Unlike the ABX_3-type OIHPs, the A_2BX_6 OIHPs (such as K_2PtCl_6) are potentially more chemically stable because their B-site is already in the tetravalent state.[39−41]

Herein, we propose an alternative crystal model, which was vacancy-ordered double OIHPs, for novel piezoelectric material design. The chemical formula was confirmed as $TMCM_2SnCl_6$ via powder X-ray diffraction (XRD) and X-ray photoelectron spectroscopy (XPS). The large d_{33} of 137 pC/N and giant g_{33} of 980 × $10^{−3}$ V·m/N were experimentally measured for the prepared $TMCM_2SnCl_6$ crystal, which was

further confirmed by the DFT study and the outputs of PNGs. The PNGs were fabricated via sandwiching the $TMCM_2SnCl_6$@PDMS composite film into two copper electrodes, where PDMS represents poly(dimethylsiloxane). A self-powered wireless communication node (SWCN) was successfully driven by the PNG. The detailed material synthesis and device fabrication processes are shown in the Supporting Information.

$TMCM_2SnCl_6$ is a vacancy-ordered double perovskite because its 50% $[SnCl_6]^{2−}$ octahedrons are replaced by periodic vacancies, in which the asymmetric $TMCM^+$ takes the A sites (Figure 1a). This is different from the reported vacancy-ordered double perovskites with spherical symmetric cations like trimethylmethylammonium (TMA) or monovalent alkali metals (Na, K, Cs, etc.) taking the A sites.[42−44] Figure 1b shows the XRD measured from the $TMCM_2SnCl_6$ single crystals (black curve) in comparison to the simulated XRD (red curve) from the projected structure in Figure 1a. The single crystal of $TMCM_2SnCl_6$ with a length of 1.8 cm is shown in Figure 1c. The agreement of XRD peaks confirms the crystal structure and its high phase purity. The $TMCM_2SnCl_6$ was aged to 6 months in an ambient atmosphere, and the XRD results are shown in Figure S1a. The reflection peaks of $TMCM_2SnCl_6$ remained almost unchanged, and no new reflection peaks appeared. These indicate the $TMCM_2SnCl_6$ crystals have not degraded into other chemicals and exhibit good stability. The $TMCM_2SnCl_6$ also exhibits good thermal stability, as indicated by a negligible change in the measured permittivity at 340 K for 1 h (Figure S 1d). The chemical states of $(TMCM)_2SnCl_6$ were measured via XPS in Figure S2. The
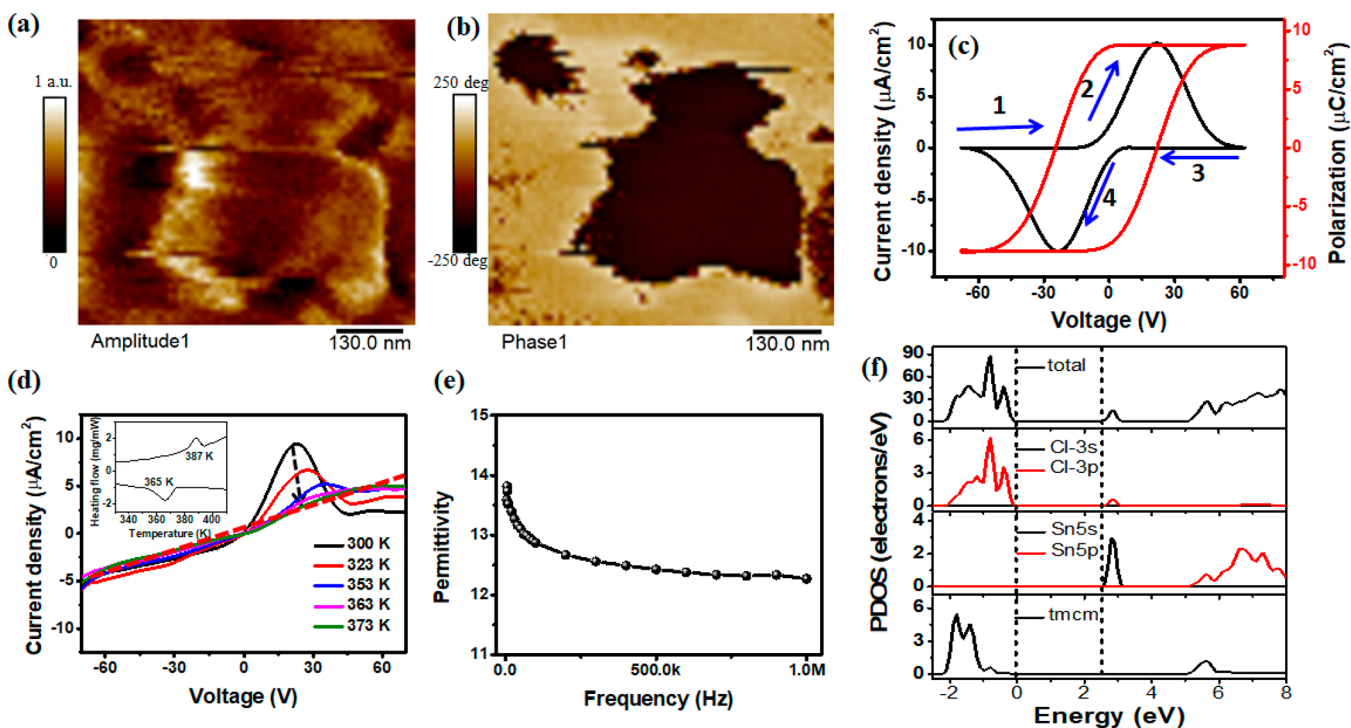
Figure 2. Piezoelectric and ferroelectric properties of $TMCM_2SnCl_6$ double perovskite: vertical PFM amplitude (a) and phase (b) images; (c) current density–voltage (J–V) curve and the integrated polarization–voltage (P–V) hysteresis loop of the $TMCM_2SnCl_6$ film at room temperature (25 °C) by using the double-wave method; (d) temperature-dependent J–V curves. Voltage was swept from −70 to 70 V. The inset is the differential scanning calorimetry (DSC) curves of $TMCM_2SnCl_6$ crystals with the scanning rate of 10 K/min; (c) frequency-dependent permittivity tested from 0.01 to 1 MHz; (f) calculated density of states of $TMCM_2SnCl_6$.

peaks at binding energy of 495.8 and 487.3 eV are assigned to Sn^{4+} and correspond to its $3d_{3/2}$ and $3d_{5/2}$ orbitals, respectively. The peaks at 200.6 and 198.8 eV are assigned to $2p_{1/2}$ and $2p_{3/2}$ orbitals of Cl^-. This is well consistent with the chemical states in $[SnCl_6]^{2-}$ octahedrons, where Sn is in the tetravalent state and Cl in the minus state.

A halogen bond has been considered as an efficient driving force to achieve the well-defined structures during crystal growth for piezoelectric properties.[45,46] In $TMCM_2SnCl_6$, there is a net attractive interaction between an electrophilic region associated with the Cl atom in $TMCM^+$ and the nucleophilic Cl^- in the $[SnCl_6]^{2-}$ octahedron (Figure 1d). The attractive nature of the halogen bond is determined by the bond distance (R, in the range of 2–6 Å) and the bond angle (θ, in the range of 150–180°), especially when R is shorter than the sum of van der Waals radii (~3.5 Å). The halogen bond in the $TMCM_2SnCl_6$ was reflected by Fourier transform infrared spectroscopy (FTIR) in Figure 1e. The absorption peak at 793 cm^{-1} (black line) is attributed to the stretching vibration of Cl–C bond of $TMCM^+$. For the $TMCM_2SnCl_6$, the absorption peak has a red-shift of 14 cm^{-1} to 807 cm^{-1} (red line). The red shift should be attributed to the increased force constant when the electrophilic Cl in $TMCM^+$ is attracted by the nucleophilic Cl in $[SnCl_6]^{2-}$ octahedron according to harmonic motion for the diatomic model.[47,48] The halogen bond energy was calculated by using DFT as a function of the bond distance (R) and the bond angle (θ) in Figures 1f and S3. With the decreasing of R, the calculated system energy of $TMCM^+ \cdots [SnCl_6]^{2-}$ decreases as the increased Coulomb attraction, followed by a quick increase afterward due to the dominating nuclear repulsion. The halogen bond energy is evaluated from the absolute value of

valley energy. The lowest energy of halogen bond is observed to be 0.021 hartree at a Cl⋯Cl bond distance of 3.06 Å for a certain C–Cl⋯Cl bond angle (θ = 150°). The bond energy increases from 0.021 to 0.024 hartree (dash line) as θ increases from 150° to 180°.

The d_{33} of $TMCM_2SnCl_6$ perovskites was measured to be 137 pC/N by using a quasi-static method in Figure S4. The ferroelectric domains were confirmed by a clear contrast in amplitude and phase images of vertical piezoelectric force microscopy (V-PFM) in Figure 2a-b. There was no crosstalk between the topography (Figure S5b) and the V-PFM phase. Meanwhile, the lateral PFM (L-PFM) was recorded in Figure S5c,d where the signal strength was found relatively weak, indicating that the spontaneous polarization was almost along the out-of-plane direction.[33] The P–V hysteresis loop was measured for $TMCM_2SnCl_6$ films with the thickness of 400 μm by using the double-wave method (DWM) in Figure 2c.[49,50] The arrows in the J–V curve indicate the voltage sweep directions (−60 V → 0 V → 60 V → 0 V → −60 V). The J–V curve exhibits two apparent current peaks at the ferroelectric switching voltage of ±23 V. The E_c of $TMCM_2SnCl_6$, expressed by the ratio of switching voltage to the film thickness, is 0.6 kV/cm. This value is comparable to that of conventional piezo-ceramics such as bulk BTO single crystals (1 kV/cm).[51] The P_s from the P–V hysteresis loop is up to 8.7 μC/cm², close to the calculated value of 8.4 ± 0.3 μC/cm². When the temperature is higher than T_c, the ferroelectric material will undergo a phase transition and lose its spontaneous polarization. The phase transition of $TMCM_2SnCl_6$ was considered from orthorhombic to cubic, as indicated by some disappearing diffraction peaks at around 26.3°, 33.5°, and 36.5° in temperature-dependent XRD
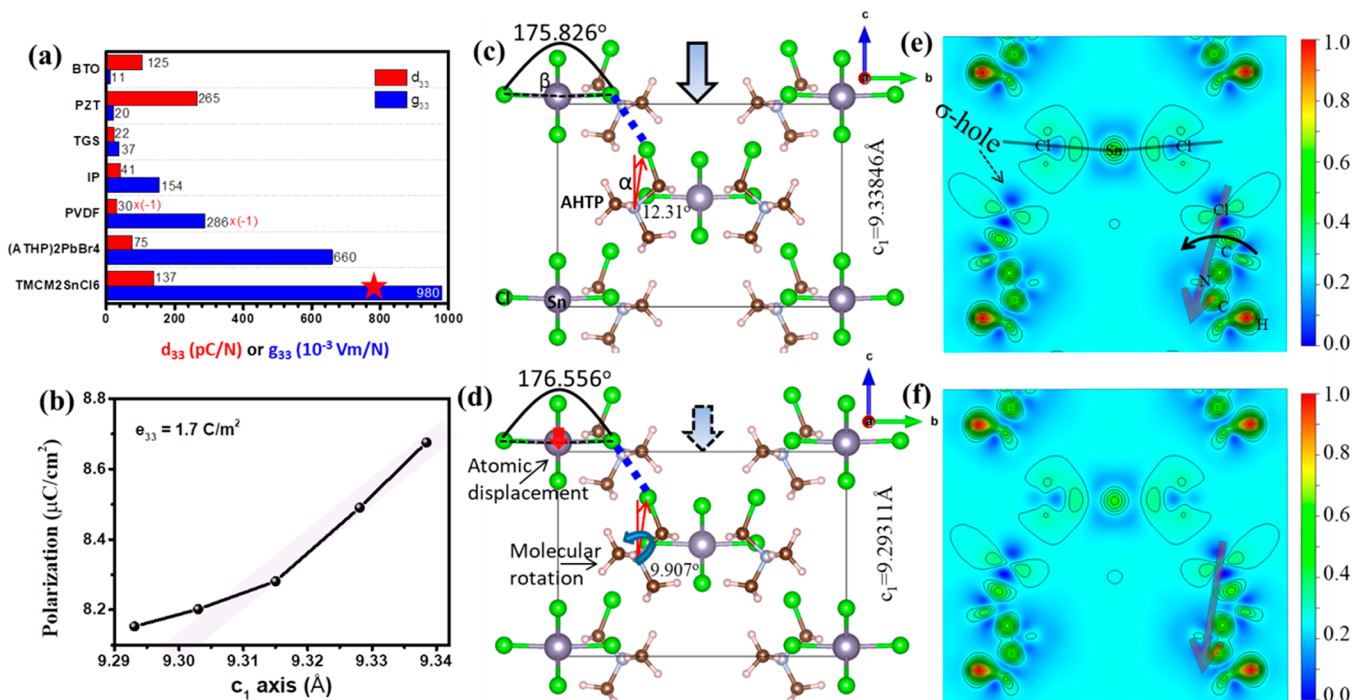
Figure 3. Origin of piezoelectricity in the $TMCM_2SnCl_6$ double perovskite: (a) the d_{33} and g_{33} of $TMCM_2SnCl_6$ compared with the reported inorganic and molecular materials, including BTO, PZT, triglycine sulfate (TGS), imidazolium perchlorate (IP), PVDF, and $(ATHP)_2PbBr_4$; (b) the calculated polarization as a function of c_1 by using Berry phase method; (c) side views of the unstrained structure and (e) corresponding deformation charge density for $c = 9.33864$ Å; (d) the strained structure and (f) deformation charge density for $c = 9.29311$ Å. The above deformation charge density is in the $[001]$ planes including the Sn−Cl···Cl−C chain. The blue and red colors represent the electron loss and gain, respectively.

(Figure S1b). The T_c of $TMCM_2SnCl_6$ was studied via monitoring the change of peak intensity at 23 V in the temperature-dependent $J-V$ curves. As indicated in Figure 2d, the current peaks disappear when the temperature rises to 353−363 K. This is consistent with a pair of thermal anomalies at 365/387 K in the differential scanning calorimetry (DSC) curves (the inset of Figure 2d) and an increase at 350−380 K in the temperature-dependent permittivity (Figure S1c). The $TMCM_2SnCl_6$ possesses a T_c above room temperature, making it suitable for PNG applications. The ε_r of perovskite oxide ceramics, such as PZT, is observed in the thousands, which stems from the hopping polaron within semiconducting grains and interfacial polarization at the insulating grain boundary.[52] The $TMCM_2SnCl_6$ exhibits a relative low ε_r of 14−12 with the frequency from 0.01 to 1 MHz in Figure 2e. This should be attributed to the insulating properties of $TMCM_2SnCl_6$, where the calculated bandgap of above 3.2 eV and a narrow conduction bandwidth are defined by the 5s orbits of Sn and the 3p orbits of Cl, as indicated in Figures 2f and S6. According to $g_{33} = d_{33}/(\varepsilon_0 \times \varepsilon_r)$, where ε_0 is the permittivity of free space and $\varepsilon_r = 16$, the calculated g_{33} is 980×10^{-3} V·m/N. Notably, a higher ε_r was chosen to match the following PNG working frequency at 40 Hz. In comparison to traditional metal oxides and other molecular materials listed in Figure 3a (or Table S1), the $TMCM_2SnCl_6$ perovskites are more favorable for the PNG applications because of both the large d_{33} and giant g_{33}.

To investigate the piezoelectric origin of $TMCM_2SnCl_6$ double perovskites, the polarization (P_{total}) was calculated by the Berry phase method as a function of c_1, where c_1 is the lattice constant during the applied strain along the c axis (Figure 3b). The slope of the linear P_{total} versus c_1 curve yields

the piezoelectric stress coefficient (e_{33}).[53,54] By fitting the P_{total} versus c_1/c_0 curve in Figure 3b, e_{33} is evaluated as 1.7 C/m². According to the calculated elastic modulus tensor ($c_{33} = 187.7$ kBar) in Table S2, the d_{33} is calculated as 90 pC/N by using the expression of $d_{33} = e_{33}/c_{33}$. The calculated d_{33} is lower than the experimental value of 137 pC/N as the P_{total} contribution resulting from lateral strain was neglected.[55] Panels c and d of Figure 3 show the crystal structure (side view) of unstrained $TMCM_2SnCl_6$ with a lattice constant c_1 of 9.33846 Å and that of strained $TMCM_2SnCl_6$ with c_1 of 9.29311 Å (corresponding to a strain of −0.4%), respectively. Under the applied strain, the angle (α) in the dipole direction of TMCM⁺ with respect to c axis decreases from 12.31° to 9.907°. According to the equation of $P_{TMCM} = \mu \times \cos(\alpha)/V_u$, where μ is the dipole moment of TMCM⁺ (4.65 D) and V_u is the cell volume, the polarization from the TMCM⁺ increases when α decreases. The deformation charge density profiles of the unstrained and strained crystal are shown in panels e and f of Figure 3, respectively. The Cl atom in TMCM⁺ is involved in the formation of the covalent bond. In addition, there is a region of lower electron density (σ-hole) where the potential is positive, which generates a cap of depleted electron density on the elongation of the covalent bond. Thus, a halogen-bonding interaction will be formed between the Cl of TMCM⁺ and the electron-rich Cl atoms in $[SnCl_6]^{2-}$. Therefore, the rotation of TMCM⁺ can trigger the atomic displacement in $[SnCl_6]^{2-}$ octahedrons simultaneously, indicated by the increased angle (β) of Cl−Sn−Cl in $[SnCl_6]^{2-}$ octahedrons from 175.6° to 176.5°. The polarization from $[SnCl_6]^{2-}$ is calculated by the equation of $P_{Sn} = P_{total} - P_{TMCM}$. Via fitting the decomposed polarization P_{TMCM} and P_{Sn} in Figure S7, the e_{33} of $[SnCl_6]^{2-}$ and TMCM⁺ is 1.5 C/m² and 0.2 C/m², respectively. It is clear
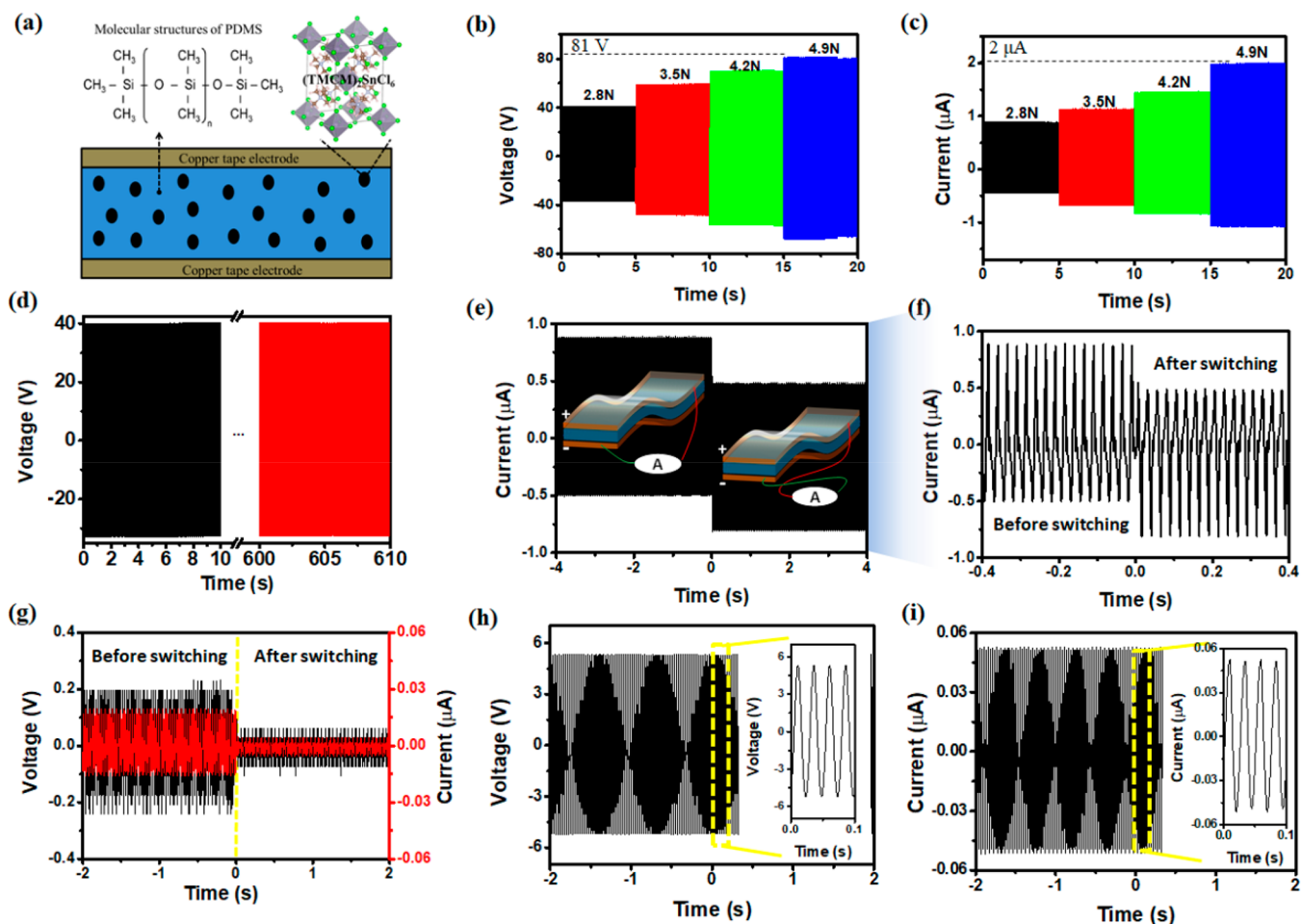
Figure 4. The piezoelectric output of single PNG: (a) device structure of PNGs via inserting TMCM$_2$SnCl$_6$@PDMS composite film between copper electrodes; (b) V_{oc} and (c) I_{sc} of PNGs with the force from 2.8 to 4.9 N (40 Hz); (d) the device reliability tested for 10 min; (e) I_{sc} and (f) enlarged view of the PNGs under forward and reverse electrical connections. The inset is schematic diagrams of the PNGs under forward and reverse connections; (g) polarity switching test of V_{oc} (black curve) and I_{sc} (red curve) of pure PDMS-based devices; (h) V_{oc} and (i) I_{sc} of PNGs based on TMCM$_2$SnCl$_6$@PDMS film (without poling). For panels d−i, the applied mechanical excitation is (2.8 N, 40 Hz).

that the $[SnCl_6]^{2-}$ contributes nearly all of the piezoelectricity. After replacing the asymmetric TMCM$^+$ by spherically symmetric TMA$^+$, the $[SnCl_6]^{2-}$ in TMA$_2$SnCl$_6$ is not distorted (Figure S8). The polarization from TMA$_2$SnCl$_6$ is 0 and not changed under an applied strain, indicated the loss of piezoelectricity. Unlike the traditional perovskite ceramics where the piezoelectricity is primarily arising from the atomic displacement (Figure S9), (i) the organic TMCM$^+$ in TMCM$_2$SnCl$_6$ can break its crystal symmetry and (ii) the piezoelectricity in TMCM$_2$SnCl$_6$ is from the halogen bond-mediated synergistic movement of atomic displacement in inorganic $[SnCl_6]^{2-}$ octahedrons and the molecular rotation of TMCM$^+$.

The piezoelectricity in the TMCM$_2$SnCl$_6$ was further demonstrated by the outputs of fabricated PNGs. The precursor of piezoelectric composite films was prepared via dispersing 10 wt % TMCM$_2$SnCl$_6$ nanoparticles (NPs) uniformly in the PDMS by mechanical stirring (Figure S10). The size of the NPs was in the range of 200−1000 nm, as shown in the SEM images and elemental mapping (Figure S11b,c). The films were grown via drop-casting the above precursor solution on a glass substrate (Figure S11a). After the drop-casting, NPs with a larger size tended to precipitate to the

bottom of the central area rather than diffuse to the marginal area (Figure S11a,d−f). The fraction of TMCM$_2$SnCl$_6$ NPs in the composite film for the PNG integration was 18 wt % measured in the dotted circle in Figure S11d by the SEM-EDS. The film thickness at the central area was 300 μm. Finally, the TMCM$_2$SnCl$_6$@PDMS composite film was sandwiched between two copper electrodes for PNG fabrication (Figures 4a and S12) (see the experimental details in the Supporting Information).

The outputs of the TMCM$_2$SnCl$_6$@PDMS-based PNGs was measured by mounting the device on a shaker in a vertical compressing and releasing process (Figure S13). For the PNGs with 18 wt % TMCM$_2$SnCl$_6$ in the composite film, the output V_{oc} and I_{sc} of 40 V and 0.9 μA was achieved under the force of 2.8 N at a frequency of 40 Hz. The device output is reproducible as indicated by the statistical analysis of V_{oc} in Figure S14. With the applied force increased from 2.8 to 4.9 N, the piezoelectric outputs (V_{oc} and I_{sc}) of the PNGs increase linearly in Figure 4b,c. The V_{oc} and I_{sc} reach 81 V and 2 μA, respectively, at an applied force of 4.9 N. The frequency-dependent V_{oc} and I_{sc} are shown in Figure S15 as the force remains 2.8 N. Meanwhile, the device outputs were also recorded at low frequency (3 Hz) via a cylindrical hammer

mounted on a linear motor and a metallic stopper. The V_{oc} and current density (J_{sc}) were measured as 11.6 V and 1.17 μA/cm^2, respectively, at an applied pressure of 0.032 MPa (Figure S16). The concentration of TMCM$_2$SnCl$_6$ on the electricity generation capacity of the PNGs was optimized in Figure S18. The output voltage and current gradually increase to 72 V and 1.3 μA with the increasing mass fraction of TMCM$_2$SnCl$_6$ NPs up to 29 wt %, under an applied force of 2.8 N. In comparison with traditional inorganic perovskite ceramics in Table S3, the TMCM$_2$SnCl$_6$ was prepared at room temperature and the PNGs exhibit the competitive piezoelectric outputs. The reliability of the PNGs was explored by continually testing the device for 10 min, and the amplitude of the output voltage shows a negligible degradation (Figure 4d and Video S1), confirming its excellent mechanical durability. Finally, the PNGs were used as an integrated power source to meet the energy demand of practical electrical loads via harvesting energy from local environment, such as a SWCN (see the details in Figure S17 and Video S2).

To demonstrate the generated outputs originated from the piezoelectric phenomenon, the following experiments were conducted: (i) The measured current output of the PNGs switched its polarity during the electrical connection reversal (Figure 4e-f and Video S3), indicating that the outputs were produced from the PNGs. (ii) For comparison, the output V_{oc} and I_{sc} of PNGs made from pure PDMS were merely 0.2 V and 0.02 μA and lacking of the polarity-switching property in Figure 4g. The V_{oc} is enhanced with the loading TMCM$_2$SnCl$_6$ NPs in the composite film, as shown in Figure S18. These verify the claim that the high performance of PNGs is determined by the incorporation of TMCM$_2$SnCl$_6$. (iii) The effect of electrical poling on the PNG outputs was investigated (see the poling procedures in the experimental section in the Supporting Information). Compared with the outputs of unpoling PNGs (Figure 4h,i), the PNGs after poling at 4.5 kV (Figure 4b,c) exhibited drastic increase in V_{oc} (from 5.4 to 40 V) and I_{sc} (from 0.05 to 0.9 μA) under the same measurement conditions (2.8 N, 40 Hz). A detailed comparison of output voltage of PNGs measured under various applied poling fields is shown in Figure S19.

In summary, a novel vacancy-ordered double perovskite of TMCM$_2$SnCl$_6$ with a large d_{33} of 137 pC/N and giant g_{33} of 980 $\times$ 10^{-3} V·m/N was proposed for energy-harvesting applications. The TMCM$_2$SnCl$_6$ perovskite possesses a high P_s of 8.7 μC/cm^2, a high T_c of 365 K, and a low E_c of 0.6 kV/cm. The ultrahigh piezoelectricity in TMCM$_2$SnCl$_6$ is attributed to the halogen bonding-mediated synergistic movements of atomic displacement in the inorganic $[SnCl_6]^{2-}$ octahedron and the dipole alignment of organic TMCM$^+$. The piezoelectric coefficients from the TMCM$_2$SnCl$_6$ was first experimentally measured, then verified by DFT study, and finally confirmed by the piezoelectric output of the PNGs. The piezoelectric composite films were prepared by dispersing TMCM$_2$SnCl$_6$ NPs into the PDMS matrix. The peak values of V_{oc} and I_{sc} of the fabricated PNGs reached 81 V and 2 μA at an applied mechanical excitation of (4.9 N, 40 Hz). The SWCN was successfully driven by the PNG. This work not only opens the door for designing novel piezoelectric OIHPs with ultrahigh d_{33} and g_{33} but also paves the way for its real applications in self-powered electronics.

■ ASSOCIATED CONTENT

ⓈⒾ Supporting Information

The Supporting Information is available free of charge at https://pubs.acs.org/doi/10.1021/acsenergylett.0c02200.

> Experimental methods; computational details; XRD, XPS, d_{33}, and calculated band structure of TMCM$_2$SnCl$_6$ crystals; digital photograph, SEM images, and piezoelectric potential simulation of TMCM$_2$SnCl$_6$@PDMS composite films; digital photos; frequency-dependent outputs of single PNG; real application of PNG for SWCN; output performance comparison of PNGs based on PDMS matrix; table for calculated elastic modulus (PDF)
>
> Video S1: device stability (MP4)
>
> Video S2: output switching (MP4)
>
> Video S3: SWCN (MP4)
>
> Crystallographic information for TMCM$_2$SnCl$_6$ at 298 K (CIF)

■ AUTHOR INFORMATION

Corresponding Authors

Chunlei Wang − *Advanced Photonics Center, School of Electronic Science and Engineering, Southeast University, Nanjing 210096, P. R. China*; Email: wangchl@seu.edu.cn

Dayan Ban − *Waterloo Institute for Nanotechnology and Department of Electrical and Computer Engineering, University of Waterloo, Waterloo N2L 3G1, ON, Canada; School of Physics and Electronics, Henan University, Kaifeng, Henan, P. R. China*; Email: dban@uwaterloo.ca

Authors

Guangguang Huang − *Waterloo Institute for Nanotechnology, University of Waterloo, Waterloo N2L 3G1, ON, Canada;* ⓄRCID orcid.org/0000-0002-3019-5270

Asif Abdullah Khan − *Waterloo Institute for Nanotechnology, University of Waterloo, Waterloo N2L 3G1, ON, Canada*

Md Masud Rana − *Waterloo Institute for Nanotechnology, University of Waterloo, Waterloo N2L 3G1, ON, Canada;* ⓄRCID orcid.org/0000-0002-8026-9821

Chao Xu − *Waterloo Institute for Nanotechnology, University of Waterloo, Waterloo N2L 3G1, ON, Canada*

Shuhong Xu − *Advanced Photonics Center, School of Electronic Science and Engineering, Southeast University, Nanjing 210096, P. R. China*

Resul Saritas − *Department of Systems Design Engineering, University of Waterloo, Waterloo N2L 3G1, ON, Canada*

Steven Zhang − *Waterloo Institute for Nanotechnology, University of Waterloo, Waterloo N2L 3G1, ON, Canada*

Eihab Abdel-Rahmand − *Department of Systems Design Engineering, University of Waterloo, Waterloo N2L 3G1, ON, Canada*

Pascal Turban − *Univ Rennes, CNRS, IPR (Institut de Physique de Rennes) - UMR 6251, F-35000 Rennes, France*

Soraya Ababou-Girard − *Univ Rennes, CNRS, IPR (Institut de Physique de Rennes) - UMR 6251, F-35000 Rennes, France*

Complete contact information is available at: https://pubs.acs.org/10.1021/acsenergylett.0c02200

Notes

The authors declare no competing financial interest.

REFERENCES

(1) Pan, C.; Zhai, J.; Wang, Z. L. Piezotronics and Piezo-phototronics of Third Generation Semiconductor Nanowires. *Chem. Rev.* **2019**, *119* (15), 9303−9359.

(2) Kim, I.; Roh, H.; Yu, J.; Jayababu, N.; Kim, D. Boron Nitride Nanotube-Based Contact Electrification-Assisted Piezoelectric Nanogenerator as a Kinematic Sensor for Detecting the Flexion-Extension Motion of a Robot Finger. *ACS Energy Lett.* **2020**, *5* (5), 1577−1585.

(3) Niu, X.; Jia, W.; Qian, S.; Zhu, J.; Zhang, J.; Hou, X.; Mu, J.; Geng, W.; Cho, J.; He, J.; Chou, X. High-Performance PZT-Based Stretchable Piezoelectric Nanogenerator. *ACS Sustainable Chem. Eng.* **2019**, *7* (1), 979−985.

(4) Biswas, P.; Hoque, N. A.; Thakur, P.; Saikh, M. M.; Roy, S.; Khatun, F.; Bagchi, B.; Das, S. Highly Efficient and Durable Piezoelectric Nanogenerator and Photo-power cell Based on CTAB Modified Montmorillonite Incorporated PVDF Film. *ACS Sustainable Chem. Eng.* **2019**, *7* (5), 4801−4813.

(5) Pandey, R.; Sb, G.; Grover, S.; Singh, S. K.; Kadam, A.; Ogale, S.; Waghmare, U. V.; Rao, V. R.; Kabra, D. Microscopic Origin of Piezoelectricity in Lead-Free Halide Perovskite: Application in Nanogenerator Design. *ACS Energy Lett.* **2019**, *4* (5), 1004−1011.

(6) Deutz, D. B.; Mascarenhas, N. T.; Schelen, J. B. J.; de Leeuw, D. M.; van der Zwaag, S.; Groen, P. Flexible Piezoelectric Touch Sensor by Alignment of Lead-Free Alkaline Niobate Microcubes in PDMS. *Adv. Funct. Mater.* **2017**, *27* (24), 1700728.

(7) Gao, X.; Zheng, M.; Yan, X.; Fu, J.; Hou, Y.; Zhu, M. High Performance Piezocomposite for Flexible Device Application. *Nanoscale* **2020**, *12*, 5175−5185.

(8) Hinchet, R.; Khan, U.; Falconi, C.; Kim, S. Piezoelectric Properties in Two-Dimensional Materials: Simulations and Experiments. *Mater. Today* **2018**, *21* (6), 611−630.

(9) Li, W.; Wu, N.; Zhong, J.; Zhong, Q.; Zhao, S.; Wang, B.; Cheng, X.; Li, S.; Liu, K.; Hu, B.; Zhou, J. Theoretical Study of Cellular Piezoelectret Generators. *Adv. Funct. Mater.* **2016**, *26* (12), 1964−1974.

(10) Dutta, B.; Kar, E.; Bose, N.; Mukherjee, S. NiO@SiO$_2$/PVDF: A Flexible Polymer Nanocomposite for a High Performance Human Body Motion-Based Energy Harvester and Tactile e-Skin Mechanosensor. *ACS Sustainable Chem. Eng.* **2018**, *6* (8), 10505−10516.

(11) Lee, J.-H.; Yoon, H.-J.; Kim, T. Y.; Gupta, M. K.; Lee, J. H.; Seung, W.; Ryu, H.; Kim, S.-W. Micropatterned P(VDF-TrFE) Film-Based Piezoelectric Nanogenerators for Highly Sensitive Self-Powered Pressure Sensors. *Adv. Funct. Mater.* **2015**, *25* (21), 3203−3209.

(12) Mao, Y.; Zhao, P.; McConohy, G.; Yang, H.; Tong, Y.; Wang, X. Sponge-Like Piezoelectric Polymer Films for Scalable and Integratable Nanogenerators and Self-Powered Electronic Systems. *Adv. Energy Mater.* **2014**, *4* (7), 1301624.

(13) Pi, Z.; Zhang, J.; Wen, C.; Zhang, Z.-b.; Wu, D. Flexible Piezoelectric Nanogenerator Made of Poly(vinylidenefluoride-co-trifluoroethylene) (PVDF-TrFE) Thin Film. *Nano Energy* **2014**, *7*, 33−41.

(14) Meng, X.; Wen, X.; Qin, G. DFT Study on Elastic and Piezoelectric Properties of Tetragonal BaTiO$_3$. *Comput. Mater. Sci.* **2010**, *49* (4), S372−S377.

(15) Jeong, C. K.; Kim, I.; Park, K. I.; Oh, M. H.; Paik, H.; Hwang, G. T.; No, K.; Nam, Y. S.; Lee, K. J. Virus-Directed Design of a Flexible BaTiO$_3$ Nanogenerator. *ACS Nano* **2013**, *7* (12), 11016−25.

(16) Zhang, G.; Liao, Q.; Zhang, Z.; Liang, Q.; Zhao, Y.; Zheng, X.; Zhang, Y. Novel Piezoelectric Paper-Based Flexible Nanogenerators Composed of BaTiO$_3$ Nanoparticles and Bacterial Cellulose. *Adv. Sci.* **2016**, *3* (2), 1500257.

(17) Wu, W.; Bai, S.; Yuan, M.; Qin, Y.; Wang, Z. L.; Jing, T. Lead Zirconate Titanate Nanowire Textile Nanogenerator for Wearable Energy-Harvesting and Self-Powered Devices. *ACS Nano* **2012**, *6* (7), 6231−5.

(18) Bowen, C. R.; Kim, H. A.; Weaver, P. M.; Dunn, S. Piezoelectric and Ferroelectric Materials and Structures for Energy Harvesting Applications. *Energy Environ. Sci.* **2014**, *7* (1), 25−44.

(19) Yan, Y.; Zhou, J. E.; Maurya, D.; Wang, Y. U.; Priya, S. Giant Piezoelectric Voltage Coefficient in Grain-Oriented Modified PbTiO$_3$ Material. *Nat. Commun.* **2016**, *7*, 13089.

(20) Li, W.; Wang, Z.; Deschler, F.; Gao, S.; Friend, R. H.; Cheetham, A. K. Chemically Diverse and Multifunctional Hybrid Organic-Inorganic Perovskites. *Nat. Rev. Mater.* **2017**, *2* (3), 16099.

(21) Zhao, X. G.; Yang, J. H.; Fu, Y.; Yang, D.; Xu, Q.; Yu, L.; Wei, S. H.; Zhang, L. Design of Lead-Free Inorganic Halide Perovskites for Solar Cells via Cation-Transmutation. *J. Am. Chem. Soc.* **2017**, *139* (7), 2630−2638.

(22) Xiao, Z.; Meng, W.; Wang, J.; Mitzi, D. B.; Yan, Y. Searching for Promising New Perovskite-Based Photovoltaic Absorbers: the Importance of Electronic Dimensionality. *Mater. Horiz.* **2017**, *4* (2), 206−216.

(23) Huang, G.; Wang, C.; Xu, S.; Zong, S.; Lu, J.; Wang, Z.; Lu, C.; Cui, Y. Postsynthetic Doping of MnCl$_2$ Molecules into Preformed CsPbBr$_3$ Perovskite Nanocrystals via a Halide Exchange-Driven Cation Exchange. *Adv. Mater.* **2017**, *29* (29), 1700095.

(24) Manser, J. S.; Saidaminov, M. I.; Christians, J. A.; Bakr, O. M.; Kamat, P. V. Making and Breaking of Lead Halide Perovskites. *Acc. Chem. Res.* **2016**, *49* (2), 330−8.

(25) Bernasconi, A.; Malavasi, L. Direct Evidence of Permanent Octahedra Distortion in MAPbBr$_3$ Hybrid Perovskite. *ACS Energy Lett.* **2017**, *2* (4), 863−868.

(26) Kim, Y.-J.; Dang, T.-V.; Choi, H.-J.; Park, B.-J.; Eom, J.-H.; Song, H.-A.; Seol, D.; Kim, Y.; Shin, S.-H.; Nah, J.; Yoon, S.-G. Piezoelectric Properties of CH$_3$NH$_3$PbI$_3$ Perovskite Thin Films and Their Applications in Piezoelectric Generators. *J. Mater. Chem. A* **2016**, *4* (3), 756−763.

(27) Jella, V.; Ippili, S.; Eom, J.-H.; Pammi, S. V. N.; Jung, J.-S.; Tran, V.-D.; Nguyen, V. H.; Kirakosyan, A.; Yun, S.; Kim, D.; Sihn, M. R.; Choi, J.; Kim, Y.-J.; Kim, H.-J.; Yoon, S.-G. A Comprehensive Review of Flexible Piezoelectric Generators Based on Organic-Inorganic Metal Halide Perovskites. *Nano Energy* **2019**, *57*, 74−93.

(28) Shahrokhi, S.; Gao, W.; Wang, Y.; Anandan, P. R.; Rahaman, M. Z.; Singh, S.; Wang, D.; Cazorla, C.; Yuan, G.; Liu, J. M.; Wu, T. Emergence of Ferroelectricity in Halide Perovskites. *Small Methods* **2020**, *4* (8), 2000149.

(29) Khan, A. A.; Rana, M. M.; Huang, G.; Mei, N.; Saritas, R.; Wen, B.; Zhang, S.; Voss, P.; Rahman, E.-A.; Leonenko, Z.; Islam, S.; Ban, D. Maximizing Piezoelectricity by Self-Assembled Highly Porous Perovskite-Polymer Composite Films to Enable the Internet of Things. *J. Mater. Chem. A* **2020**, *8* (27), 13619−13629.

(30) Ippili, S.; Jella, V.; Kim, J.; Hong, S.; Yoon, S. G. Unveiling Predominant Air-Stable Organotin Bromide Perovskite toward Mechanical Energy Harvesting. *ACS Appl. Mater. Interfaces* **2020**, *12* (14), 16469−16480.

(31) Jella, V.; Ippili, S.; Yoon, S.-G. Halide (Cl/Br)-Incorporated Organic-Inorganic Metal Trihalide Perovskite Films: Study and Investigation of Dielectric Properties and Mechanical Energy Harvesting Performance. *ACS Appl. Electron. Mater.* **2020**, *2* (8), 2579−2590.

(32) Liao, W. Q.; Zhao, D.; Tang, Y. Y.; Zhang, Y.; Li, P. F.; Shi, P. P.; Chen, X. G.; You, Y. M.; Xiong, R. G. A Molecular Perovskite Solid Solution with Piezoelectricity Stronger Than Lead Zirconate Titanate. *Science* **2019**, *363* (6432), 1206−1210.

(33) You, Y. M.; Liao, W. Q.; Zhao, D.; Ye, H. Y.; Zhang, Y.; Zhou, Q.; Niu, X.; Wang, J.; Li, P. F.; Fu, D. W.; Wang, Z.; Gao, S.; Yang, K.; Liu, J. M.; Li, J.; Yan, Y.; Xiong, R. G. An Organic-Inorganic Perovskite Ferroelectric with Large Piezoelectric Response. *Science* **2017**, *357* (6348), 306−309.

(34) Chen, X. G.; Song, X. J.; Zhang, Z. X.; Li, P. F.; Ge, J. Z.; Tang, Y. Y.; Gao, J. X.; Zhang, W. Y.; Fu, D. W.; You, Y. M.; Xiong, R. G. Two-Dimensional Layered Perovskite Ferroelectric with Giant Piezoelectric Voltage Coefficient. *J. Am. Chem. Soc.* **2020**, *142* (2), 1077−1082.

(35) Deswal, S.; Singh, S. K.; Pandey, R.; Nasa, P.; Kabra, D.; Praveenkumar, B.; Ogale, S.; Boomishankar, R. Neutral 1D Perovskite-Type ABX_3 Ferroelectrics with High Mechanical Energy Harvesting Performance. *Chem. Mater.* **2020**, *32* (19), 8333−8341.

(36) Zhang, Z. X.; Zhang, H. Y.; Zhang, W.; Chen, X. G.; Wang, H.; Xiong, R. G. Organometallic-Based Hybrid Perovskite Piezoelectrics with a Narrow Band Gap. *J. Am. Chem. Soc.* **2020**, *142* (41), 17787−17794.

(37) Zhang, Y.; Song, X.-J.; Zhang, Z.-X.; Fu, D.-W.; Xiong, R.-G. Piezoelectric Energy Harvesting Based on Multiaxial Ferroelectrics by Precise Molecular Design. *Matter* **2020**, *2* (3), 697.

(38) Vijayakanth, T.; Ram, F.; Praveenkumar, B.; Shanmuganathan, K.; Boomishankar, R. Piezoelectric Energy Harvesting from a Ferroelectric Hybrid Salt $[Ph_3MeP]_4$ $[Ni(NCS)_6]$ Embedded in a Polymer Matrix. *Angew. Chem., Int. Ed.* **2020**, *59* (26), 10368−10373.

(39) Morss, L. R.; Carnall, W. T.; Williams, C. W.; Fahey, J. A.; Fuger, J.; Meyer, G.; Irmler, M. Syntheses and X-ray Diffraction Studies of $[N(CH_3)_4]_2BkCl_6$ and $[N(CH_3)_4]_2ZrCl_6$; Absorption Spectrum of Bk^{4+} in $[N(CH_3)_4]_2BkCl_6$. *J. Less-Common Met.* **1991**, *169* (1), 1−8.

(40) Karim, M. M. S.; Ganose, A. M.; Pieters, L.; Winnie Leung, W. W.; Wade, J.; Zhang, L.; Scanlon, D. O.; Palgrave, R. G. Anion Distribution, Structural Distortion, and Symmetry-Driven Optical Band Gap Bowing in Mixed Halide Cs_2SnX_6 Vacancy Ordered Double Perovskites. *Chem. Mater.* **2019**, *31* (22), 9430−9444.

(41) Maughan, A. E.; Ganose, A. M.; Almaker, M. A.; Scanlon, D. O.; Neilson, J. R. Tolerance Factor and Cooperative Tilting Effects in Vacancy-Ordered Double Perovskite Halides. *Chem. Mater.* **2018**, *30* (11), 3909−3919.

(42) Fedorovskiy, A. E.; Drigo, N. A.; Nazeeruddin, M. K. The Role of Goldschmidt's Tolerance Factor in the Formation of A_2BX_6 Double Halide Perovskites and its Optimal Range. *Small Methods* **2020**, *4* (5), 1900426.

(43) Autillo, M.; Wilson, R. E. Phase Transitions in Tetramethylammonium Hexachlorometalate Compounds $(TMA)_2MCl_6$ (M = U, Np, Pt, Sn, Hf, Zr). *Eur. J. Inorg. Chem.* **2017**, *2017* (41), 4834−4839.

(44) Tan, Z.; Li, J.; Zhang, C.; Li, Z.; Hu, Q.; Xiao, Z.; Kamiya, T.; Hosono, H.; Niu, G.; Lifshitz, E.; Cheng, Y.; Tang, J. Highly Efficient Blue-Emitting Bi-Doped Cs_2SnCl_6 Perovskite Variant: Photoluminescence Induced by Impurity Doping. *Adv. Funct. Mater.* **2018**, *28* (29), 1801131.

(45) Hua, X. N.; Liao, W. Q.; Tang, Y. Y.; Li, P. F.; Shi, P. P.; Zhao, D.; Xiong, R. G. A Room-Temperature Hybrid Lead Iodide Perovskite Ferroelectric. *J. Am. Chem. Soc.* **2018**, *140* (38), 12296−12302.

(46) Liao, W. Q.; Tang, Y. Y.; Li, P. F.; You, Y. M.; Xiong, R. G. Competitive Halogen Bond in the Molecular Ferroelectric with Large Piezoelectric Response. *J. Am. Chem. Soc.* **2018**, *140* (11), 3975−3980.

(47) Cavallo, G.; Metrangolo, P.; Milani, R.; Pilati, T.; Priimagi, A.; Resnati, G.; Terraneo, G. The Halogen Bond. *Chem. Rev.* **2016**, *116* (4), 2478−601.

(48) Huang, G.; Wang, C.; Zhang, H.; Xu, S.; Xu, Q.; Cui, Y. Post-Healing of Defects: an Alternative Way for Passivation of Carbon-Based Mesoscopic Perovskite Solar Cells via Hydrophobic Ligand Coordination. *J. Mater. Chem. A* **2018**, *6* (6), 2449−2455.

(49) Fukunaga, M.; Noda, Y. New Technique for Measuring Ferroelectric and Antiferroelectric Hysteresis Loops. *J. Phys. Soc. Jpn.* **2008**, *77* (6), No. 064706.

(50) Hu, L.; Dalgleish, S.; Matsushita, M. M.; Yoshikawa, H.; Awaga, K. Storage of an Electric Field for Photocurrent Generation in Ferroelectric-Functionalized Organic Devices. *Nat. Commun.* **2014**, *5*, 3279.

(51) Trithaveesak, O.; Schubert, J.; Buchal, C. Ferroelectric Properties of Epitaxial $BaTiO_3$ Thin Films and Heterostructures on Different Substrates. *J. Appl. Phys.* **2005**, *98* (11), 114101.

(52) Han, H.; Voisin, C.; Guillemet-Fritsch, S.; Dufour, P.; Tenailleau, C.; Turner, C.; Nino, J. C. Origin of Colossal Permittivity in $BaTiO_3$ via Broadband Dielectric Spectroscopy. *J. Appl. Phys.* **2013**, *113* (2), No. 024102.

(53) Liu, S.; Zheng, F.; Grinberg, I.; Rappe, A. M. Photoferroelectric and Photopiezoelectric Properties of Organometal Halide Perovskites. *J. Phys. Chem. Lett.* **2016**, *7* (8), 1460−5.

(54) Shi, J.; Grinberg, I.; Wang, X.; Rappe, A. M. Atomic Sublattice Decomposition of Piezoelectric Response in Tetragonal $PbTiO_3$, $BaTiO_3$, and $KNbO_3$. *Phys. Rev. B: Condens. Matter Mater. Phys.* **2014**, *89* (9), 094105.

(55) Tholander, C.; Abrikosov, I. A.; Hultman, L.; Tasnádi, F. Volume Matching Condition to Establish the Enhanced Piezoelectricity in Ternary $(Sc,Y)_{0.5}(Al,Ga,In)_{0.5}N$ Alloys. *Phys. Rev. B: Condens. Matter Mater. Phys.* **2013**, *87* (9), No. 094107.